Radiatively driven downdrafts and redshifts in transition region lines: - I. Reference model

F. Reale, G. Peres, S. Serio

Istituto e Osservatorio Astronomico, Palazzo dei Normanni, 90134 Palermo, Italy
E-mail: reale@oapa.astropa.unipa.it, peres@oapa.astropa.unipa.it, serio@oapa.astropa.unipa.it

Astronomy & Astrophysics, 1996, in press

Abstract

We show that downdrafts driven by radiatively-cooling subarcsecond perturbations in the solar transition region can produce significant UV line redshifts consistent with those frequently observed on the solar disk, and, by extension, with those more recently observed on stars. We model in detail the thermo-hydrodynamic evolution of a non-linear isobaric spherical condensation inside an initially hydrostatic atmosphere, stratified both in density and temperature, and with initial conditions typical of a solar active region. We study the evolution of the atmosphere both neglecting the effect of magnetic fields and taking it into account by forcing conduction and motions to be only along the vertical direction. The synthesis of emitted flux and effective speed in four UV lines from model results shows the presence of intense redshifted components at speeds between 5 and 10 km/s.

Subject headings: Stars: atmospheres – Sun: transition region – Stars: UV radiation

1 Introduction

The presence of red-shifts in UV lines is a well established observational fact both for the Sun and for some stars. Solar observations with spectrometers aboard rockets and satellites, e.g. OSO8 (Lites et al. 1976), S082B/Skylab (Doschek, Feldman and Bohlin 1976), UVSP/SMM (Gebbie et al. 1981, Athay et al. 1983), HRTS (Dere 1982, Dere, Bartoe and Brueckner 1984, 1986, Athay and Dere 1989, Kjeldseth-Moe et al. 1993, Brekke 1993), LASP EUV (Rottman et al. 1990, Hassler, Rottman and Orral 1991), have extensively detected descending subsonic motions between 5 and 10 km/s in some important UV lines, forming mostly between 5 10^4 K and 5 10^5 K. Some studies have even mapped the dependence of downward speed on line temperature (Dere 1982, Achour et al. 1995), finding a peak around 10 km/s at 10^5 K. Stellar observations with sufficient spectral resolution have been made recently with GHRS/HST (Linsky, Wood and Andrulis 1993, Linsky and Wood 1995) and also show redshifts above 5 km/s on a variety of stars.

A full explanation of such red-shifts is still missing, although several hypotheses, as recently summarized by Brekke (1993), have been proposed so far: they include the return of spicular material, siphon flows in coronal loops, nano-flares, a different temporal duration of upflows and downflows, and asymmetric heating of coronal loops. None of them has been found entirely satisfactory.

In this work we show that the observed redshifts may be caused by downdrafts which develop in the transition region and are driven by radiatively cooling condensations. There has been a sizable amount of work on the thermal stability of perturbations in gravitationally stratified coronal atmospheres (e.g. Field 1965, Defouw 1970, Malagoli, Rosner & Bodo 1987, Malagoli, Rosner & Fryxell 1990, Hattori & Habe 1990, Reale et al. 1991, hereafter R91, Reale, Serio & Peres 1994, hereafter RSP) which has provided the basic conceptual framework and insight required to study gravitationally and thermally stratified atmospheres, a more realistic model of proper stellar upper atmospheres, which we tackle in the following. In RSP we have shown that in an isothermal model atmosphere, moderate isobaric condensations whose size is of the order of one arcsec could become thermally unstable in the temperature range typical of the solar transition region ($10^5 < T < 10^6$ K), even under the stabilizing influence of plasma isotropic thermal conduction. RSP have also pointed out the importance of these results in understanding the redshifted lines formed at the transition region temperature.

Since the transition region, however, is characterized by a steep temperature and density gradient, a realistic study of thermal instabilities in the transition region requires to extend the stability analysis to atmospheres with both density and temperature stratification.

In the present work we consider a detailed model of the transition region and chromosphere, initially in hydrostatic equilibrium and energy balance, and we illustrate the fundamental processes which eventually bring to the formation of red-shifted lines. In particular we analyze in detail the evolution of one specific, but fairly representative, non-linear spherical isobaric perturbation in the transition region of an active region loop, by means of a hydrodynamic two-dimensional numerical model. Analytical works (e.g. Defouw 1970) are not helpful and cannot be compared to the present results, nor they can provide estimates for observations, because they do not account for highly non-linear perturbations as well as strong atmospheric stratification of density and temperature, as we consider here. In a forth-coming work we will generalize our study by exploring the space of the relevant control parameters, both of the unperturbed atmosphere and of the perturbation, in order to constrain the validity of the proposed scenario and to provide a broader quantitative framework.

Our task is directly aimed at obtaining diagnostics amenable to comparisons with real observations; to this end we have evaluated several features of the evolving plasma including the time-resolved synthesis of the emission.

In section 2 we describe the hydrodynamic numerical model, the hydrostatic atmosphere and the condensation that perturbs it, and our synthesis of line emission and Doppler-shifts from model results; in section 3 we report our results computed by assuming isotropic thermal conduction; in section 4 we illustrate the effects of an ambient magnetic field; in section 5 we discuss the results and draw our conclusions.

2 The reference model

2.1 The code

We have used the same two-dimensional hydrodynamic code as in RSP, based on an improved Flux Corrected Transport (FCT) scheme (e.g. Boris & Book 1976, Boris, Book & Zalesak 1981, Kössl & Müller 1988) described in Reale, Peres & Serio (1990) and in R91, and now including the description of thermal conduction (Reale 1995) according to Spitzer (1962). Our implementation of the FCT code links the well-known ability of FCT schemes to describe shock fronts and steep gradients, to the absence of terracing, which instead typically affects other FCT schemes, and to a good computational efficiency (for instance relatively long time steps, corresponding to a Courant number 0.7 has been used in the present calculations), as shown by an extensive testing (Reale et al. 1990). The code has been designed in wide generality to work in a variety of geometries, and to be appropriate to study many different astrophysical systems.

The code numerically solves the following hydrodynamic time-dependent equations:

$$\frac{\partial n}{\partial t} + \nabla \cdot (n\mathbf{v}\ ) = 0\,, \tag{1}$$

$$\frac{\partial (n\mathbf{v}\ )}{\partial t} + \nabla \cdot (n\mathbf{v}\ \mathbf{v}\ ) = -\frac{1}{m}\nabla p + n\mathbf{g}\ \ , \tag{2}$$

$$\frac{\partial u}{\partial t} + \nabla \cdot [(u+p)\mathbf{v}\ ] = mn\mathbf{g}\ \cdot \mathbf{v}\ - n^2 P(T) + \mathcal{H}(\mathbf{r}\ ) + \nabla F_c\,, \tag{3}$$

where

$$u = \frac{1}{2}mnv^2 + \mathcal{E}\,, \qquad p = (\gamma - 1)\mathcal{E}\,,$$

$$T = \frac{p}{2kn}\,, \qquad F_c = -\kappa T^{5/2}\nabla T$$

n is the particle volume density, t is the time, $\mathbf{v}$ is the plasma bulk velocity, p the pressure, m is the average mass per particle ($m = 2.1\ 10^{-24}$ g for solar abundance), g the gravity acceleration, $P(T)$ the radiative losses per unit emission measure, $\mathcal{H}$ the volumetric heating, T the local plasma temperature, F_c is the heat flux, κ is the plasma thermal conductivity (assumed isotropic in the equations above), and $\gamma = 5/3$. The radiative losses function vs temperature can be described as a piece-wise power law $P(T) = \beta T^\alpha$, where the constants β and α assume different values in different temperature ranges, as prescribed in Rosner et al. (1978) and Peres et al. (1982), $\mathcal{H}$, the volumetric heating, is discussed in section 2.2.

Equations (1) and (2) are solved according to our FCT scheme. The energy equation (3) is solved with the technique of *time-splitting*, i.e. in two separate phases, one solving the hydrodynamic equations, the other the thermal balance between thermal conduction, heating and radiative losses; they use different algorithms and integration time steps (e.g. Richtmyer & Morton 1967). In the first phase, the energy equation is solved using an implicit scheme in alternating directions (Richtmyer and Morton 1967), which ensures the unconditional numerical stability of the solution. In this case the integration time step is dictated by the local radiation and conduction characteristic times. The equations with the hydrodynamic terms are integrated using the FCT scheme on time steps determined by the Courant condition. For a detailed description of the implementation of this technique see Reale (1995).

In the present problem we use cylindrical coordinates: Z, perpendicular to the sun's surface, and r; we assume rotational symmetry around the Z-axis. In this geometry the center of spherical perturbations is on the Z axis ($r = 0$).

The present version of the code computes the numerical solutions on a fixed spatial grid, defined at the beginning of each model simulation. In order to describe the steep vertical gradients of the solar (or stellar) transition region with reasonable resolution, we have set the vertical grid spacing progression Δz_i along the Z direction in such a way that Δz_i is minimum ($2\ 10^4$ cm) at the base of the transition region and then increases both upwards (i.e. in the transition region and corona) and downwards (in the chromosphere). In Section 2.2 we provide further details on the structure of the initial atmosphere. The rate of the increase of the spacing has been chosen in such a way that the initial temperature in the profile does not change more than 20 % between two adjacent points along Z.

Along the radial direction r the spacing is uniform in an inner region, which extends radially from the Z-axis to a distance much larger than the radius of the initial perturbation. The spatial resolution along r in this region is such that the radius of the initial perturbation encompasses at least 10 grid points. Outside this internal region the radial grid spacing expands with a geometric progression, of ratio 1.2.

The computational spatial domain is always much larger than the geometric size of the initial perturbation, and the outer radial boundaries are placed so far from the perturbation ($R_{max} = 2.1\ 10^7$ cm, namely seven times the perturbation radius), that the boundary conditions do not affect significantly the evolution of the perturbation and of the nearby plasma, over the time lapses considered. We have fixed all physical quantities at the lower and upper boundaries of the stratified atmosphere, as in R91 and in RSP, and considered reflection boundaries on the inner vertical boundary ($r = 0$), and zero-gradient conditions on the $r = R_{max}$ outer boundary.

We first study the evolution of a model perturbation in the presence of isotropic thermal conduction. Then we explore also possible modifications to this scheme due to the magnetic fields, known to be present in the atmosphere, by examining the evolution of the perturbation in the presence of a non-isotropic thermal conduction, preferentially directed along the vertical direction, i.e. along the most likely field lines, and a purely one-dimensional model simulating the possibility that the magnetic field inhibits any motion across the field lines, and therefore any kind of buoyant evolution.

2.2 The initial unperturbed atmosphere

As in the previous works (R91, RSP), the ambient atmosphere is initially steady and stratified. The novelty of the present approach is that we are now considering a more realistic model of solar atmosphere, accounting both for density and temperature stratification along Z. In particular the initial unperturbed atmosphere is the corona and transition region calculated according to the coronal loop model of Serio et al. (1981). We consider a loop with base pressure 3 dyne cm^{-2}, typical of an active region loop. The atmosphere stratification is determined by solving the detailed mass, hydrostatic and energy equations, including the effects of gravity, heat conduction, and radiative losses, and with a uniform steady heating.

The base of the transition region has been carefully matched to a chromospheric model taken from those of Vernazza, Avrett and Loeser (1981). The lower boundary is located at 7000 K. The chromosphere is in hydrostatic equilibrium with the upper atmosphere.

The energy balance of the steady unperturbed atmosphere is ensured by the heating function $\mathcal{H}$ in equation (3) (Peres et al. 1982). More specifically, this steady-state heating function is temperature-dependent: it is uniform for $T > 2\ 10^4$ K, and non-uniform for $T < 2\ 10^4$ K, i.e. in the chromosphere. This heating function ensures the thermal stability of the unperturbed atmosphere (Peres et al. 1982).

We are not interested in the details of the evolution of the plasma of the lower layers of the atmosphere, since redshifts are formed in higher temperature lines. For this reason we have neglected the effect of the partial plasma ionization at temperatures below $2\ 10^4$ K, and therefore assumed that the whole atmosphere is composed of fully ionized plasma.

The stratification of the hydrostatic atmosphere is described according to a gravity acceleration varying with height as $g = g_\odot \cos[\pi z/(2L)]$, as in a semicircular coronal loop of semilength $L = 10^9$ cm, with feet perpendicular to the solar surface. We note that, since the loop is much longer than the transition region, the gravity is vertical in the region we are more interested in here, namely the transition region.

For this study, the temperature range of interest is $2\ 10^4 - 10^6$ K. We will not discuss in detail the evolution of our atmosphere outside this temperature range, although the whole atmosphere we model spans temperatures between 7000 K and few 10^6 K.

The atmosphere computed according to Serio et al. (1981) has been interpolated on the grid described in the previous section and has been let relax for a time (> 1000 s) long enough to let even minor readjustments settle, and reach a configuration highly stable for the code and, at the same time, still realistic as atmosphere description. We have also verified *a posteriori* that the maximum fluid speed resulting from numerical noise at the end of this relaxation is negligible with respect to the relevant speeds involved in the evolution of the perturbations we have studied.

2.3 The perturbation

As we did in RSP, we consider a spherical isobaric condensation but in a different ambient atmosphere. Consequently we have to revise the definition of the space of the relevant control parameters. In RSP we had four control parameters: i) the local pressure, ii) the temperature T_0 of the atmosphere isothermal before the perturbation, iii) the initial density contrast of the perturbation δ, the fractional difference of density with respect to the unperturbed medium (for isobaric perturbations this is the inverse of the fractional difference of temperature), iv) the radius R of the perturbation.

The thermal stratification of the atmosphere requires a different definition of the parameter T_0. Since it is no longer possible to define a single temperature of the background atmosphere, we will define T_0 as the temperature of the unperturbed atmosphere *at the center* of the perturbation. It is worth noting that, since the temperature increases monotonically from the chromosphere to the corona, when we assign T_0 we also assign a specific height in the atmosphere.

In Fig. 1 we report, for our loop with base pressure 3 dyne cm^{-2}, the height above the chromosphere top (located where $T = 2\ 10^4$ K) vs plasma temperature. In the same figure, we show for comparison the critical radius, which separates thermally stable (region below the dashed curve) from unstable perturbations, as determined from the isothermal linear analysis (RSP). The two curves are quite similar, which is not surprising because both are governed by the interplay of conduction and radiation. However the height above the chromosphere is systematically *lower* than the critical size, implying that linear perturbations in the transition region and in corona are expected to be stable, and that thermal instability, if any, is expected only in the highly non-linear regime ($\delta >> 0$). From the same figure we note also that perturbations to be potentially unstable should be large as compared to their distance from the top of the chromosphere, i.e. they should extend vertically over most of the transition region. Such perturbations are far from being isothermal, but involve a significant temperature structure. We will consider one such perturbation all contained in the transition region, and, therefore, of relatively small size ($<< 1$ arcsec).

We will follow the evolution of the perturbation as long as it stays inside the transition region, but not after it penetrates the chromosphere. Its extension over most of the transition region implies that the space below the perturbation down to the base of the transition region is very small. The time taken by a downflowing cell to cross this thin layer is small as well: distances of the order of 10^7 cm, the thickness of our transition region, at a speed of $\sim 10^6$ cm/s, typical of observed redshifts, will be covered in ~ 10 s. Therefore we expect the perturbation to evolve on such short time scales, much shorter than the typical evolution times of the cases reported in RSP.

In summary, we will identify our perturbation with the following four control parameters: i) the loop base pressure, ii) the temperature of the unperturbed atmosphere at the location of the center of the perturbation, iii) the initial density contrast of the perturbation δ, iv) the radius R of the perturbation, which can also be conveniently expressed as fraction of the height of the center of the perturbation above the chromosphere R/R_M.

Summarizing the features of the problem described in this section, the initial atmosphere is typical of an active region loop with base pressure 3 dyne cm^{-2}, the perturbation is initially spherical and isobaric, and the temperature of the plasma at its center before the perturbation proper is $T_0 = 4.5\ 10^5$ K, the radius is $R = 0.75\ R_M = 3\ 10^6$ cm, and therefore the bottom of the perturbation is $\approx 10^6$ cm above the base of the transition region, covering the temperature range $2.9\ 10^5 < T < 5.4\ 10^5$ K; its density is initially twice as large as that of the unperturbed medium, i.e. $\delta = 1$. The initial setup is shown in Fig. 2, where we report the relevant quantities vs height at $r = 0$.

2.4 The synthesis of line emission and effective speed

In order to have a quantitative evaluation of the amount and intensity of the Doppler-shifts expected from the proposed model, we have synthesized the time-resolved line emission and an effective speed weighted by the emission from the computed plasma evolution.

We have considered the following four resonance UV lines among the most representative ones (e.g. Brekke 1994), whose temperatures of maximum emissivity (given in brackets) span in the temperature range of the transition region: Si IV 1402.77 Å($7\ 10^4$ K), C IV 1548.20 Å(10^5 K), O IV 1401.16 Å($1.4\ 10^5$ K), O V 1371.30 Å($2.4\ 10^5$ K). In Fig.3 we show, for each of these lines, the plasma emissivity vs plasma temperature $G(T)$, computed according to Landini & Monsignori Fossi (1990).

Along the evolution of our perturbation, we have computed the evolution of the emitted flux $F(r,t)$ in each of the four UV lines, integrated along the loop. Since the UV lines are emitted only in the very thin transition region, near the base of the loop, this is equivalent to integrate along the line of sight:

$$F(r,t) = \int_0^{z_{max}} n^2(r,z,t)\ G(T(r,z,t))\ dz \tag{4}$$

Analogously we have computed an effective vertical speed as an average velocity weighted by emission in the line:

$$v_{ze}(r,t) = \frac{\int_0^{z_{max}} v_z(r,z,t)\ n^2(r,z,t)\ G(T(r,z,t))\ dz}{\int_0^{z_{max}} n^2(r,z,t)\ G(T(r,z,t))\ dz} \tag{5}$$

The effective velocity provides a plausible measure of the Doppler shift of the selected UV line caused by the plasma motions in the considered volume.

Our aim is now to evaluate the contribution of Doppler-shifted emission with respect to the emission of the unperturbed hydrostatic medium. In the light of our ignorance of the temporal and spatial spectrum of the perturbations, we are not able to integrate the emission over some observation time and field of view. Therefore, to have a quantitative estimate of the amount and intensity of the Doppler-shifted components, we have computed the average flux F_{avg} from each line component with velocity v_{ze} as:

$$F_{avg}(v_{ze}) = \frac{\int_{t_0}^{t_{end}} \int_0^{r_{max}} F(r,t,v_{ze}) 2\pi\ r(v_{ze})\ dr\ dt}{\int_{t_0}^{t_{end}} \int_0^{r_{max}} 2\pi\ r(v_{ze})\ dr\ dt} \quad . \tag{6}$$

In this study we have neglected the effects of ionization non-equilibrium when computing the emission in the UV lines. This assumption may not be entirely appropriate, since the times for reaching ionization equilibrium may be comparable to the characteristic times of evolution, especially in lower pressure loops. We defer to forth-coming works for a detailed evaluation of this effect.

3 The results

3.1 The evolution

The sequence of grey scale pictures of Fig. 4 describes the evolution of the density contrast and of the velocity field in the region around the perturbation, in the first 3 seconds, in the assumption of isotropic thermal conduction.

At the beginning the outer shells of the perturbation expand, driven by thermal conduction. Expansion is stronger in the upper half of the bubble ($v \approx 16$ km/s in the upper shells, at t = 0.2 s), because there the ambient temperature is higher, and conduction more efficient, than below, thus leading to a more efficient leveling of ambient temperature, and, ultimately, to an overpressure.

The expansion causes a rapid decrease of both the temperature and density contrast, most at the top of the condensation. After t = 0.4 s, the top of the perturbation has practically disappeared, and what is left of the condensation is confined in the lower half of the initial bubble. Once again, this is a sign of the substantial thermal stability of the corona.

The density contrast increases around the center of the perturbation ($\delta \approx 2$, at t = 0.2 s). The region of maximum density contrast then shifts downwards reaching the base of the transition region at $t \sim 2.4$ s. Since it has moved by $\approx 3\ 10^6$ cm, the average downward propagation speed is $\gtrsim 10$ km/s. This speed is significantly higher than the downward plasma bulk speed ($v_z \leq 7$ km/s), implying that *this downward displacement of the dense core is not the effect* *of a gravitational downflow, but instead the propagation of a thermal front.* On one hand the condensation is progressively eroded from above by the action of thermal conduction, on the other hand the density progressively increases below the initial perturbation because less heat is conducted from above and the plasma cools down (and its density increases) rapidly. The maximum density contrast increases monotonically in this time lapse, and reaches a maximum of $\delta \approx 10$ at t = 3 s, at the base of the transition region.

As for the velocity evolution, after the initial radial motion has decayed, at $t \sim 0.8$ s, the velocity field starts to be dominated by downward motions with speed values around 6-8 km/s. After t = 2.6 s, when the condensation has reached the base of the transition region, the velocity in all the field rapidly decreases ($v \sim 3$ km/s).

We have followed the evolution of the system until $t = 6$ s, when any motion has decreased to the level of numerical noise, although a slight, and very thin indeed, overdensity is still present at the base of the transition region. As we show in the following, at t = 6 s there is no significant contribution to the emission of our four selected UV lines in excess of the background.

3.2 The line emission and effective vertical speed

We have computed the emitted flux $F(r,t)$ and the effective vertical speed $v_{ze}(r,t)$, for each of the four UV lines, in the first 6 seconds of evolution, according to definitions (4) and (5). We show our results in Fig. 5 as grey scale pictures of both quantities vs r, the radial distance from the loop axis, (X coordinate) and time (Y coordinate). In the velocity pictures contour lines separate upward (positive values) from downward (negative values) flow regions.

All the pictures show a common pattern: we find localized high value (black) regions both in intensity and (downward) velocity pictures. For each line the high values of flux and velocity occur almost simultaneously.

Therefore, the plasma emits intensely in the spectral lines and at the same time the radiation is expected to be more redshifted than at any other time. In all lines this occurs within the first 3 seconds, earlier in oxygen lines (at $t \sim 0.5$ s), and later in the two softer lines (at $t \sim 2.5$ s), and close to $r = 0$, the region where the perturbation evolves. Outside this region, and at later times, the emission is much lower and the effective velocity is generally below 1 km/s.

As a consequence of this scenario we expect *a very intense redshifted component in all these lines during the evolution of such a perturbation*, because redshifted emission is also more intense than that from the unperturbed *static* atmosphere. The maximum downward effective speeds are quite similar in the four UV lines and decrease slightly from harder to softer lines (5.0 km/s for the Si IV line, 6.5 km/s for CIV, 7.9 km/s for O IV, 7.5 km/s for O V).

Fig. 6 shows the average contribution of the Doppler-shifted components to the emission in the four UV lines $F_{avg}(v)$, as defined in section 2.4. The flux in each speed bin is reported in units of the average flux from the static component. It is clear that the most intense emission comes from the downward moving components at high speed ($|v_{ze}| > 4$ km/s) in all the lines: once again, *redshifted components are expected to provide the most intense emission.* Upward moving components are at low speed and emit at low flux levels.

The maximum flux value is much larger than the static component in all lines and decreases slightly from softer to harder lines: 10.4 for Si IV line, 9.5 for C IV, 6.7 for O IV, 5.7 for OV.

4 Effects of magnetic fields

In the presence of magnetic fields, we expect the evolution of the perturbations to be somehow different. First of all, conduction will occur only along the field lines, thus its thermally stabilizing effect will be lower and the efficiency of downdrafts production will be higher. Moreover, the motion of the plasma would be confined along the field lines. We have explored the evolution of perturbations using one-dimensional conduction as well as one-dimensional conduction and hydrodynamics, in order to evaluate the extent to which the general pattern of our results could be changed by the presence of magnetic fields.

4.1 Non-isotropic conduction

We have computed the evolution of the same perturbation in the same conditions as in section 3, except that we have forced zero thermal conduction along the radial r direction, therefore allowing conduction only along the Z direction.

This assumption attenuates somehow the efficiency of thermal conduction, thus we expect the perturbation to cool and collapse more easily than with isotropic conduction. In Fig.7 we report the bubble evolution, in a form directly comparable to that in Fig.4.

The lowered efficiency of thermal conduction has quite significant effects. We still have an initial outward radial motion, although weaker than before ($v \leq 10$ km/s for $t < 1$ s). The evolution is not substantially different from that of the isotropic case in the first 2 seconds, except for a more evident flow converging to the $r = 0$ axis at the base of the transition region. The converging flow is due to the depression formed because the base of the transition region is underheated – less heat is conducted from above. However, at t = 2 s a thermal instability begins to develop, reaching a very high density contrast ($\delta > 10$), and the associated dense plasma core *falls by gravity*, something which did not happen with isotropic conduction. The plasma evolution is now governed by the gravitational fall, no longer by the propagation of thermal fronts. The perturbation moves with the flow and therefore more slowly than before, because the downflow average speed is lower than the thermal propagation speed. At $t = 6$ s the condensation has reduced to a thin disk, and the flow speed is quite low. The maximum density contrast is $\delta_{max} = 41$, at $t \approx 3.3$ s, and it decreases to $\delta \sim 30$ at t = 6 s.

As we did before (Fig.5), in Fig.8 we show the grey scale pictures of the emitted flux $F(r,t)$ and the effective vertical speed $v_{ze}(r,t)$.

We can identify regions of high downward speed in all lines, as we did in Fig.5. At variance from the previous case, the maximum redshift (in practice the black spot in each of the pictures at right) now occurs at the same time for all lines ($t \approx 3$ s). At such a time the thermal instability has developed and the downflow associated to the dense core is at its maximum speed just before the arrival at the base of the transition region. Effective speeds involved in the vertical motion are higher than with isotropic conduction (up to 13.5 km/s for Si IV, 12.6 km/s for C IV, 10.2 km/s for OIV, 6.8 km/s for OV).

Bright features (pictures at left) are characterized by quite different patterns: regions close to the vertical axis across the perturbation center brighten at first – and this occurs earlier for harder lines – and later the brightening moves to a thin region at $1 < r < 2\ 10^6$ cm from the central axis. This shift produces the wing-like pattern in the flux pictures. The wing is "wider" for harder lines (e.g. O V).

We note that the brightenings close to the central axis occur at times very similar to those of the isotropic conduction case. However, since the time of maximum redshifts is delayed for all lines, the time of maximum emission no longer coincides with that of maximum vertical speed, as instead it did in the case of isotropic conduction. This determines a different emission distribution of the Doppler-shifted components, shown in Fig.9 (cf.Fig.6). In particular, in all lines, the most redshifted flux components are no longer the most intense ones, i.e. the trend redshift vs brightness is no longer monotonically increasing. Instead we find a well defined emission peak at intermediate downward speeds (~ 4 km/s for Si IV, C IV and O IV, ~ 3 km/s for O V line), lower than those of the peaks for the isotropic conduction case. However, there are significant redshifted components at quite high speeds, exceeding 10 km/s in the first three lines and reaching ~ 7 km/s in the O V line.

The maximum flux contrast on the static component is lower than with isotropic conduction in the oxygen lines, comparable in C IV line, and much higher in Si IV line.

4.2 One-dimensional hydrodynamics

We have examined the evolution of a perturbation of the same intensity, vertical size and height as before, but with a purely one-dimensional model. In this configuration we describe a layered perturbation, and no horizontal/radial motions are possible.

We find that the atmosphere in practice readjusts to a new steady state after about 3.3 sec. As in the previous cases, thermal conduction smoothes out rapidly the top of the perturbation. The lower part of the perturbation drifts to the base of the transition region, with a maximum downward speed of ~ 19 km/s at $t \approx 2$ sec. There the density contrast settles to a high steady value ($\delta \sim 20$). This is equivalent to say that the transition region has slightly shifted upwards ($\sim 10^6$ cm).

In Fig.10 we show the evolution of the emitted flux $F(t)$ and the effective vertical speed $v_{ze}(t)$ in the four selected UV lines for this one-dimensional model, which can be compared to the grey scale pictures of Figs.5 and 8. Also in this case, we notice localized low speed minima, i.e. relatively short-lasting high downward speeds, in all lines, with quite high velocity values ($v_{ze} \sim 10$ km/s for Si IV line and $15 < v_{ze} < 20$ km/s for the other lines). The highest downward speeds occur practically at the same time ($t \approx 2$ s) in all lines.

Instead we notice a different timing of the emitted flux in the four lines. O V shows a fast monotonically decreasing flux already from the beginning and settles to a steady low level after ≈ 1 s. O IV shows a small peak at $t \approx 0.3$ s and then an analogous fast decrease. Both C IV and Si IV, the two softest lines, show a very prominent emission peak, the former at $t \approx 1.3$ s, the latter at $t \approx 1.6$ s. Only for Si IV the emission peak is almost synchronous to the peak of downward effective speed.

In fact in Fig. 11 we see that in Si IV the fastest downward moving emission component is also the most intense one, as it occurred in all lines in Fig.6. In the other lines we find velocity/intensity distributions analogous to those already encountered in Fig.9. The most intense component is not at the highest downward speed but at ~ 10 km/s for C IV and O IV, and at ~ 5 km/s for O V. Other significant emission components reach quite high speeds, $|v_{ze}| > 15$ km/s, in C IV, O IV and O V lines.

5 Discussion and conclusions

The scope of this work is to explore the hypothesis that dowdrafts driven by condensation formed inside the transition region can produce significant redshifts in several UV lines as those typically observed on the solar disk and also on stars. We have suggested this hypothesis already in previous studies of thermal instabilities in atmospheres with no temperature stratification (RSP). Here we have followed a more detailed and appropriate approach in order to derive qualitative and quantitative insight into the proposed model: in particular, our attempt to provide detailed emission signatures has required an accurate description of the ambient unperturbed atmosphere, realistic for an external solar and stellar atmosphere, i.e. highly stratified both in density and temperature.

The structure of the unperturbed atmosphere deserves some comments by itself: we already know, from RSP, that the region of the solar atmosphere where realistic perturbations are expected to evolve toward thermal instability is the transition region. Since the transition region is typically very thin, orders of magnitudes thinner than both the chromosphere and the corona, we expect that any perturbation will cross this region in a very short time. In fact the overall evolution times in our modeling are invariably below 10 sec, at least one order of magnitude smaller than the buoyancy time. Furthermore, initial perturbations totally enclosed in the transition region of an active region loop, as the ones we consider here, are necessarily small in size, typically below the resolution threshold of present-day instruments.

On the other hand, we have shown (Fig.1) that thermal conduction rapidly disrupts very small and weak condensations. Therefore perturbations expected to leave signatures in the observations must be both quite intense and deeply non-linear (i.e. initially $\delta >> 0$), and quite large as compared to the thickness of the transition region.

We have chosen as a reference model, here described in detail, a non-linear condensation ($\delta = 1$), almost as large as the thickness of the transition region ($R = 0.75\ R_M$) of an active region loop (base pressure 3 dyne cm^{-2}, and at a temperature above the temperature of the typically observed UV lines ($T_0 = 4.5\ 10^5$ K). This model is useful to gain an insight on the interplay of the physical mechanisms at work and on their observational signatures. The strong temperature structuring on such a small spatial scale makes the evolution of the perturbation absolutely non-trivial.

We have seen that, in the assumption of isotropic thermal conduction, the mechanism governing the evolution of the condensation is the competition between radiative cooling and thermal conduction.

Despite the condensation does not result into a proper thermal instability, the density contrast remains quite high in the low transition region where thermal conduction is not very efficient and where most of the redshifted lines are formed. Such a high density contrast, associated to a significant downflow at speed ~ 10 km/s, brings to a significant contribution of redshifted emission in lines well below 5 10^5 K for an observer looking at the solar disk. Due to the high efficiency of thermal conduction in the higher layers of the transition region we hardly expect that lines forming closer to coronal temperatures (e.g. Fe XII) show significant redshifts. Other effects of primary importance in more simplified configurations, here have no significant influence: dynamic instabilities, such as Rayleigh-Taylor and Kelvin-Helmholtz ones, and even gravity, despite at first glance it would be expected to be the major responsible for dense downflows. In other words, gravity does not necessarily play a major role to obtain intense redshifted components in the UV lines: the temperature structure of the transition region brings naturally to thermal downdrafts.

In order to understand quantitatively what redshifts we can expect and how intense can be the redshifted emission compared to the static and blueshifted ones, we have folded the results through the temperature response of four transition region lines and analyzed the emitted flux and effective speed distributions in space and time.

We have seen that, during the evolution of the condensation, the brightness of all lines in a region close to the central axis, i.e. inside the condensation itself, becomes much higher than that of the surrounding medium. From the analysis of the evolution of the effective speeds, we expect that, for this particular model, this intense line emission is redshifted. The duration of this redshifted brightening is quite short (~ 1 s). We have computed the average line flux of emission components at different Doppler-shifts during the evolution and shown that *downward speeds (redshifts) are much higher, and the corresponding emission components much more intense, than upward speeds (blueshifts)*, the highest flux coming from the most redshifted component. The speeds of the brightest components are between 5 and 8 km/s, of the same order as the most frequently observed values in the selected lines. One could also be tempted to claim that higher speeds are associated to lines at higher temperature (i.e. O lines), but a general statement on this aspect cannot be made before a proper exploration of the parameter space, described in a forth-coming work.

The results reported so far for a reference case with typical loop plasma values, and therefore fairly representative, are promising in explaining the observed redshifts with thermal downdrafts, since they are able to reproduce many of the observed features.

However, these results may be influenced by our basic assumption of isotropic thermal conduction, appropriate to a magnetic field-free atmosphere, but not always realistic, especially inside an active region loop. In particular, for the largely subsonic flows which we invariably obtain in this work, the assumption of negligible effect of the magnetic field (B) can be made as long as $|B| < (4\pi\rho)^{1/2}|v| \sim 1$ G (for $\rho \sim 2\ 10^{-13}$ g cm^{-3}, $|v| \sim 10$ km/s), a value much weaker than expected in an active region.

Actually, if one aims at generating a thermal instability, isotropic conduction is a more conservative assumption than a directional conduction, because it is more efficient in attenuating temperature gradients. On the other hand the effect of different physical assumptions on the observable quantities is not trivial. Therefore, we have also investigated the effect of conduction along the vertical direction only, and then even that of one-dimensional conduction and dynamics.

Non-isotropic conduction does, in fact, lead to a more unstable evolution, so that a proper thermal instability develops. We have noted that, due to the reduced thermal conduction, in this case gravity acquires a major role in governing the flow evolution, so that, for instance, the condensation takes longer to arrive at the base of the transition region. In spite of the more unstable and gradual evolution, apparently we do *not* derive more significant redshifts in the UV lines. The most intense emission basically comes still from components as fast as those obtained with isotropic conduction. The only qualitative difference is the presence of higher speed line components still significantly more intense than the static components, which may provide observable contributions and are distributed as high speed red-shifted tails. Such tails appear even more prominent, and up to higher speeds (~ 20 km/s), when modeling the extreme case of purely one-dimensional hydrodynamics and thermal transport.

We would like to remark however that, although the components distribution may change, *we obtain invariably the brightest line emission coming from downward moving components always in the same speed range and with values of the same order as the observed ones*, in all the three cases. It is worth noting that there are two main physical effects at work at the same time, i.e. radiative cooling vs thermal conduction and gravity, and both of them concur to produce dense downflows.

The question arises on how such non-linear perturbations are triggered in the transition region: on the basis of preliminary computations we find that they could hardly originate from episodic heating events in the coronal section of the loops, in agreement to previous studies (Hansteen 1993, but see Hansteen and Maltby 1994). The problem is that perturbations large enough to develop redshifts have a lifetime short with respect to sound crossing times. In these conditions, it is hard to imagine how consistent perturbations can be formed by hydrodynamic processes. Perturbations might instead be generated by modulation of conductive flux due to large amplitude MHD waves (see also Hansteen and Maltby 1994).

In conclusion, our reference model describes thermal downflows naturally occurring in the solar transition region (and we expect similar effects on stellar atmospheres). Our hypothesis that UV redshifts are due to dense plasma downflows in the transition region appears to be realistic and deserves further analysis. In particular the exploration of the space of the important control parameters, the ambient pressure, the size, intensity and temperature of the perturbations, will provide a much broader scenario and more detailed constraints on the validity of the model. Although our results cannot be directly compared with observations, the synthesis of line profiles integrated over a range of volumes and times may provide constraints on the spectrum, repetition time and filling factor of perturbations required to reproduce the average observations and therefore to discriminate on the mechanisms for their formation.

Acknowledgments: We acknowledge partial support from Ministero dell'Università e della Ricerca Scientifica e Tecnologica and Consiglio Nazionale delle Ricerche.

References

Achour H., Brekke P., Kjeldseth-Moe O., Maltby P., 1995, ApJ, in press.

Athay R. G., Dere K. P., 1989, ApJ, 346, 514.

Athay R. G., Gurman J. B., Henze W., 1983, ApJ, 269, 706.

Boris J.P., Book D.L. 1976, J. Comp. Phys., 20, 397.

Boris J.P., Book D.L., Zalesak S. 1981, Finite-Difference Techniques for Vectorized Fluid Dynamics Calculations, ed. Book D., Springer-Verlag (New York), 29.

Brekke P., 1993, ApJ, 408, 735.

Brekke P., 1994, Space Science Reviews, 70, 97.

Defouw R.J., 1970, ApJ, 160, 659.

Dere K. P., 1982, Sol. Phys., 77, 77.

Dere K. P., Bartoe J.-D. F., Brueckner G. E., 1984, ApJ, 281, 870.

Dere K. P., Bartoe J.-D. F., Brueckner G. E., 1986, ApJ, 305, 947.

Doschek G. A., Feldman U., Bohlin J. D., 1976, ApJ, 205, L177.

Field G.B., 1965, ApJ, 142, 531.

Gebbie K. B., et al., 1981, ApJ, L115.

Hansteen V., 1993, ApJ, 402, 741.

Hansteen V., Maltby P., 1994, Adv. Space Res., 14, (4)57.

Hattori M., Habe A., 1990, MNRAS, 242, 399.

Hassler D. M., Rottman G. J., Orrall F. Q., 1991, ApJ, 372, 710.

Kjeldseth-Moe O., Brynildsen N., Brekke P., Maltby P., Brueckner G. E., 1993, Sol. Phys., 145, 257.

Kössl D., Müller E. 1988, A&A, 206, 204.

Landini M., Monsignori Fossi B. C., 1990, A&AS, 82, 229.

Linsky J. L., Wood B. E., 1995, ApJ, in press.

Linsky J. L., Wood B. E., Andrulis C., 1993, Proceedings of Eighth Workshop on Cool Stars, Stellar Systems, and the Sun, Athens, Georgia, 11-14 October 1993, preprint.

Lites B. W., Bruner E. C. Jr., Chipman E. G., Shine R. A., Rottman G. J., White O. R., Athay R. G., 1976, ApJ, 210, L11.

Malagoli A., Rosner R., Bodo G., 1987, ApJ, 319, 632.

Malagoli A., Rosner R., Fryxell B., 1990, MNRAS, 247, 367.

Peres G., Rosner R., Serio S., Vaiana G. S., 1982, ApJ 252, 791.

Reale F., 1995, Comp. Phys. Comm., 83, 13.

Reale F., Peres G., Serio S., 1990, Nuovo Cimento B 105, 1235.

Reale F., Serio S., Peres G., 1994, ApJ, 433, 811 (RSP).

Reale F., Rosner R., Malagoli A., Peres G., Serio S., 1991, MNRAS, 251, 379 (R91).

Richtmyer R. D., Morton K. W. 1967, Difference Methods for Initial-Value Problems, Interscience (New York).

Rosner R., Tucker W. H., Vaiana G. S., 1978, ApJ, 220, 643.

Rottman G. J., Hassler D. M., Jones M. D., Orral F. Q., 1990, ApJ, 358, 693.

Serio S., Peres G., Vaiana G. S., Golub L., Rosner R., 1981, ApJ 243, 288.

Spitzer L. Jr., 1962, Physics of Fully Ionized Gases, Interscience (New York).

Vernazza J. E., Avrett E. H., Loeser R., 1981, ApJS 45, 619.

Figure Captions

Fig.1: Height (solid line) above the base of the transition region ($2\ 10^4$ K) vs temperature inside a loop model atmosphere with base pressure 3 dyne cm^{-2}. The critical perturbation radius as defined in RSP is also shown for reference (dashed line).

Fig.2: Temperature and density vs height along the central axis of the unperturbed atmosphere (thick and thin solid line, respectively), and of the isobaric perturbation (long and short dashes). We show a fraction of the atmosphere in the larger graph, and the whole atmosphere in the inset.

Fig.3: Plasma emissivity $G(T)$ vs temperature in four UV lines: Si IV 1402.77 Å(solid line), C IV 1548.20 Å(dashed line), O IV 1401.16 Å(dashed-dotted), O V 1371.30 Å(dashed-doubly dotted), as from Landini & Monsignori-Fossi (1990).

Fig.4: We show the evolution of the isobaric perturbation for isotropic thermal conduction with a sequence of grey scale pictures. The logarithm of the density contrast above the unperturbed medium and the velocity field, with the maximum speed below each picture, are shown at the times (in seconds) above each picture. Only the relevant region of the atmosphere is shown.

Fig.5: Emitted flux (left, erg cm^{-2} s^{-1}) in the four UV lines and related effective speed (right, km/s) vs the distance from the central axis (abscissa) and time (ordinate). The contours separate regions of upward (positive, marked) and downward (negative) effective speed.

Fig.6: Average emitted flux vs effective velocity in the four UV lines, computed according to equation (6).

Fig.7: Evolution as in Fig.4 but for non-isotropic thermal conduction (along Z only).

Fig.8: As in Fig.5 but for non-isotropic thermal conduction.

Fig.9: As in Fig.6 but for non-isotropic thermal conduction.

Fig.10: As in Fig.5 (and 8) for the case of one-dimensional perturbation.

Fig.11: As in Fig.6 but for the case of one-dimensional perturbation.

Fig.1

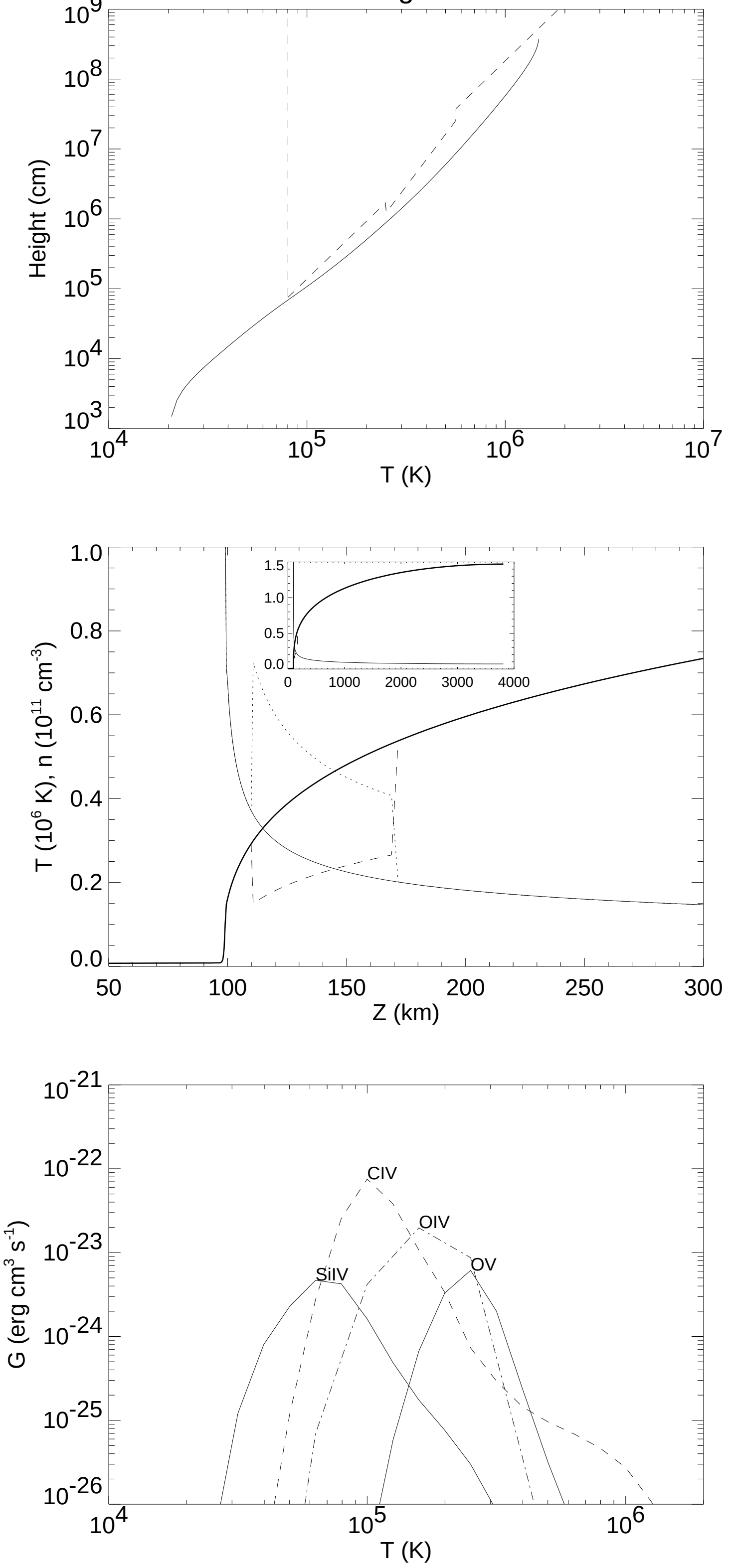

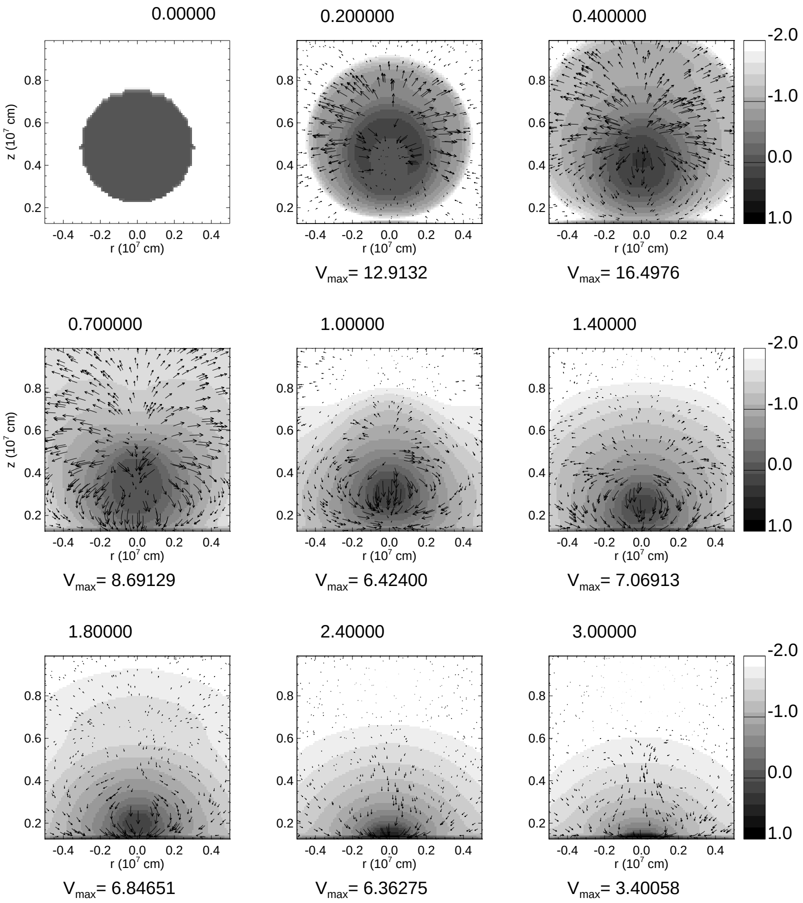

0.00000
0.200000
0.400000
0.700000
1.00000
1.40000
1.80000
2.40000
3.00000
z (10^7 cm)
r (10^7 cm)
-2.0
-1.0
0.0
1.0
V_{max}= 12.9132
V_{max}= 16.4976
V_{max}= 8.69129
V_{max}= 6.42400
V_{max}= 7.06913
V_{max}= 6.84651
V_{max}= 6.36275
V_{max}= 3.40058

Fig.4

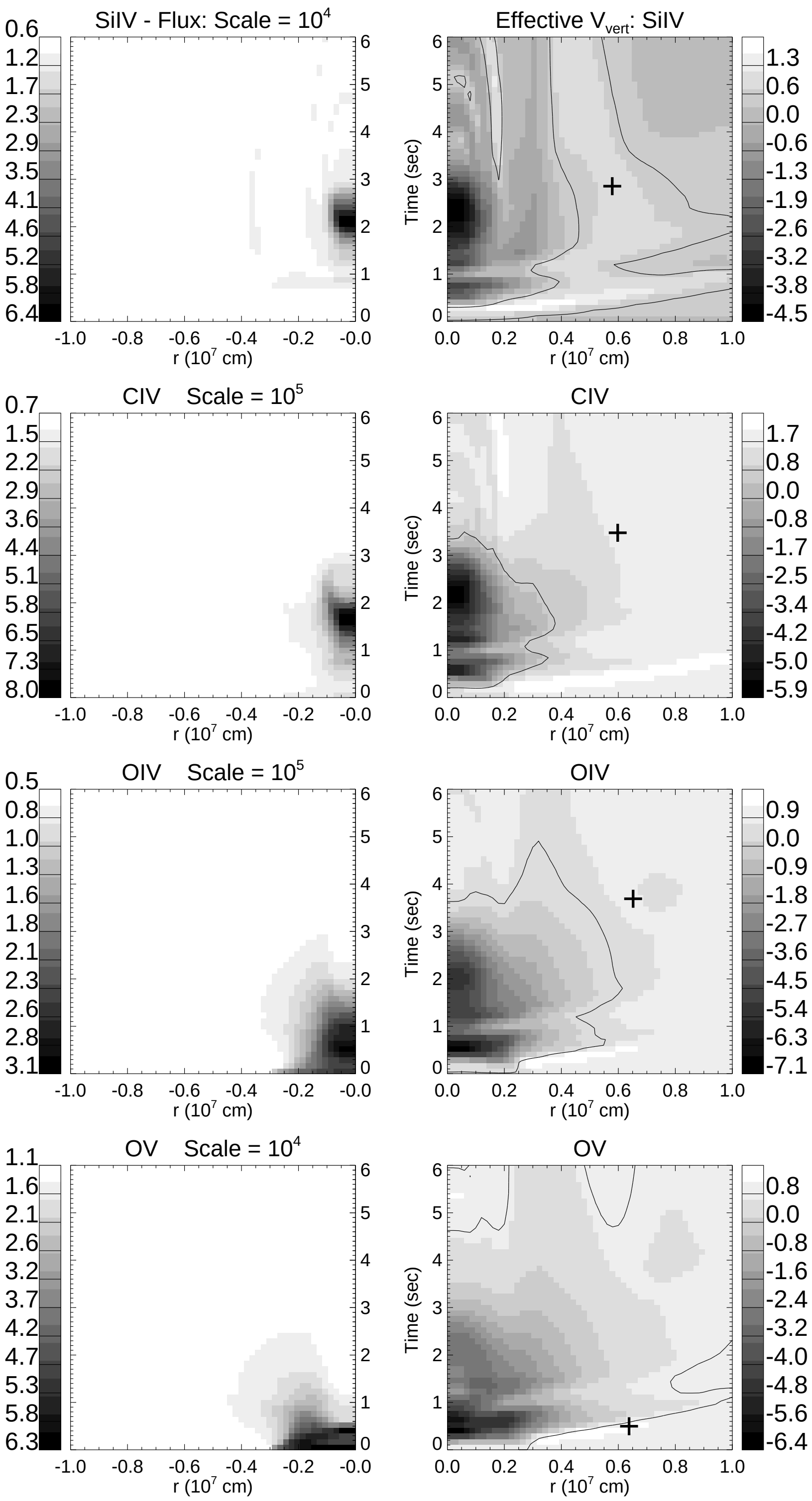
SiIV - Flux: Scale = 10^4
0.6
1.2
1.7
2.3
2.9
3.5
4.1
4.6
5.2
5.8
6.4
Effective V_vert: SiIV
1.3
0.6
0.0
-0.6
-1.3
-1.9
-2.6
-3.2
-3.8
-4.5
CIV Scale = 10^5
0.7
1.5
2.2
2.9
3.6
4.4
5.1
5.8
6.5
7.3
8.0
CIV
1.7
0.8
0.0
-0.8
-1.7
-2.5
-3.4
-4.2
-5.0
-5.9
OIV Scale = 10^5
0.5
0.8
1.0
1.3
1.6
1.8
2.1
2.3
2.6
2.8
3.1
OIV
0.9
0.0
-0.9
-1.8
-2.7
-3.6
-4.5
-5.4
-6.3
-7.1
OV Scale = 10^4
1.1
1.6
2.1
2.6
3.2
3.7
4.2
4.7
5.3
5.8
6.3
OV
0.8
0.0
-0.8
-1.6
-2.4
-3.2
-4.0
-4.8
-5.6
-6.4
Time (sec)
r (10^7 cm)

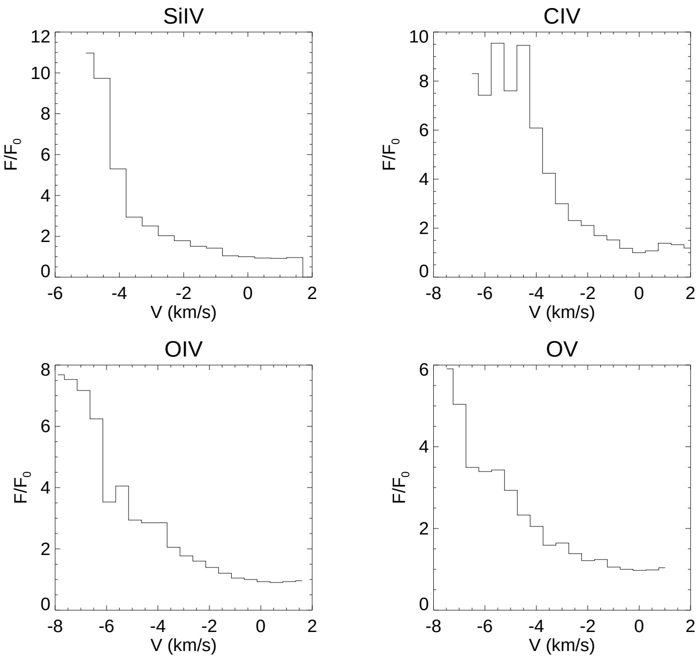
SiIV
CIV
OIV
OV
F/F0
V (km/s)

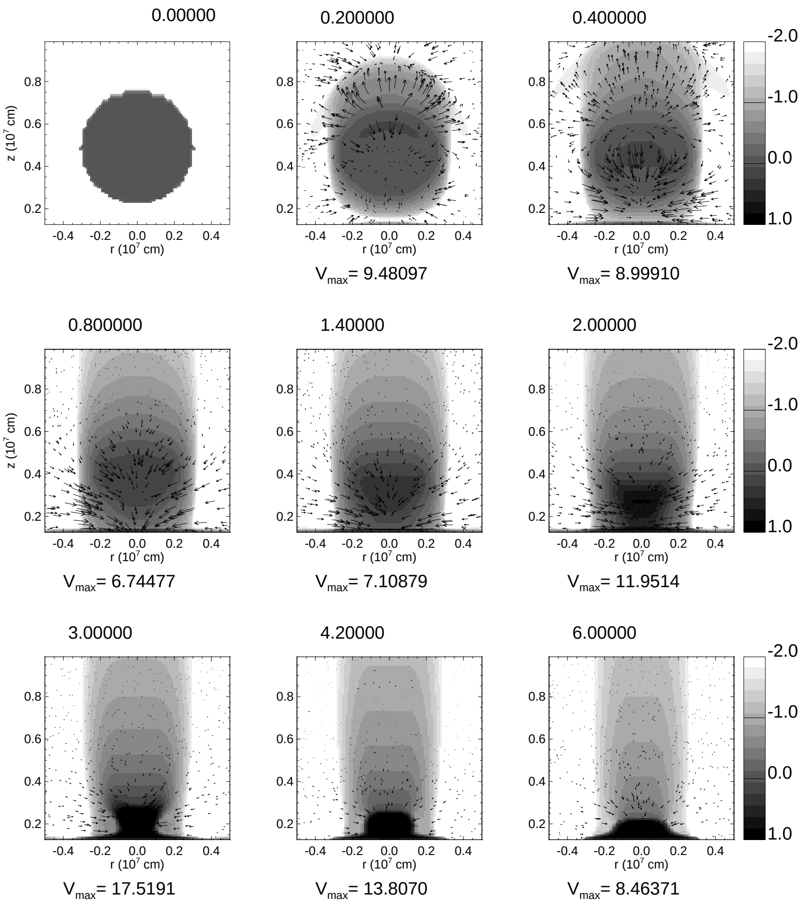
0.00000
0.200000
0.400000
0.800000
1.40000
2.00000
3.00000
4.20000
6.00000
z (10^7 cm)
r (10^7 cm)
Vmax= 9.48097
Vmax= 8.99910
Vmax= 6.74477
Vmax= 7.10879
Vmax= 11.9514
Vmax= 17.5191
Vmax= 13.8070
Vmax= 8.46371
-2.0
-1.0
0.0
1.0

Fig.7

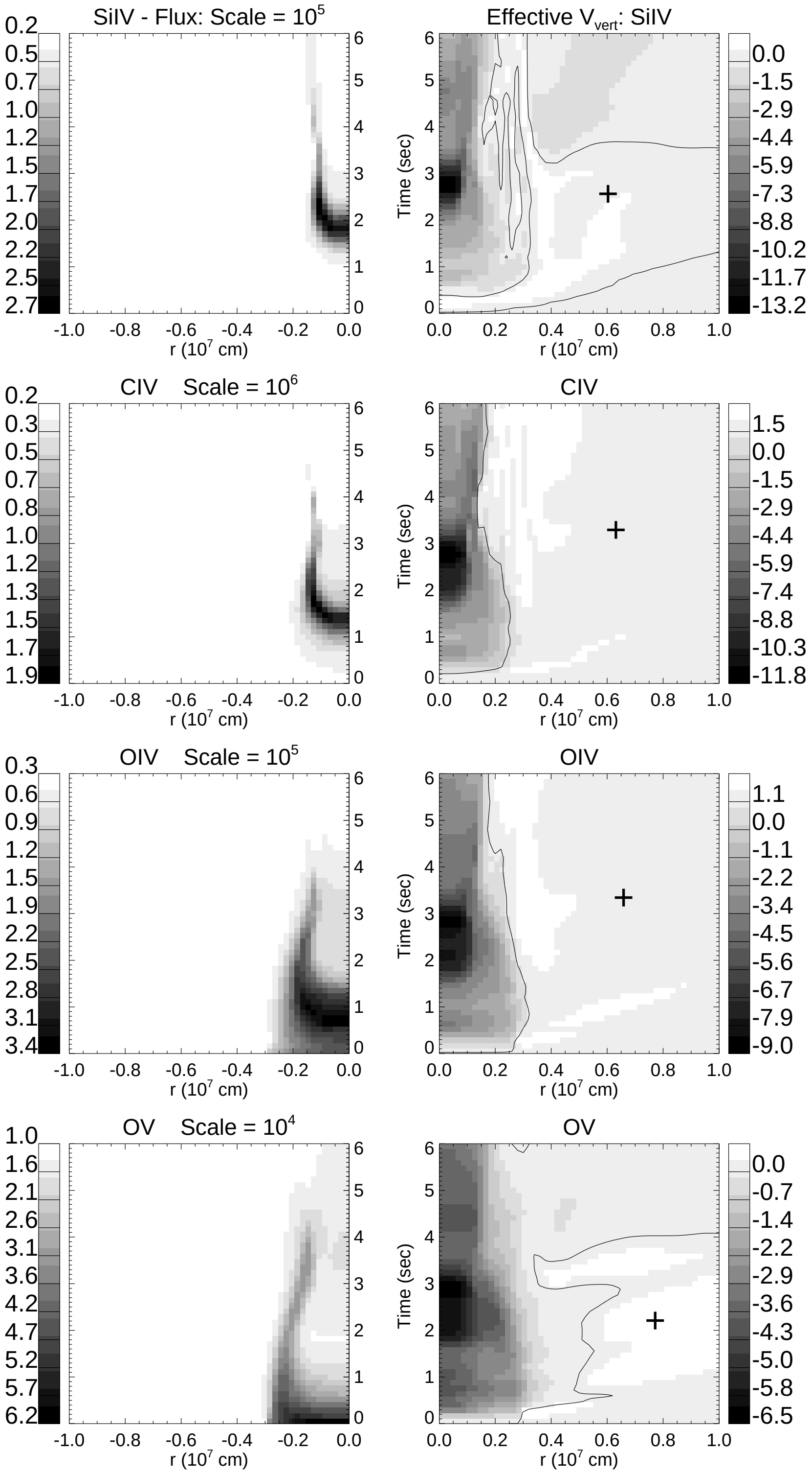

SiIV - Flux: Scale = 10^5
Effective V_vert: SiIV
CIV Scale = 10^6
CIV
OIV Scale = 10^5
OIV
OV Scale = 10^4
OV
r (10^7 cm)
Time (sec)

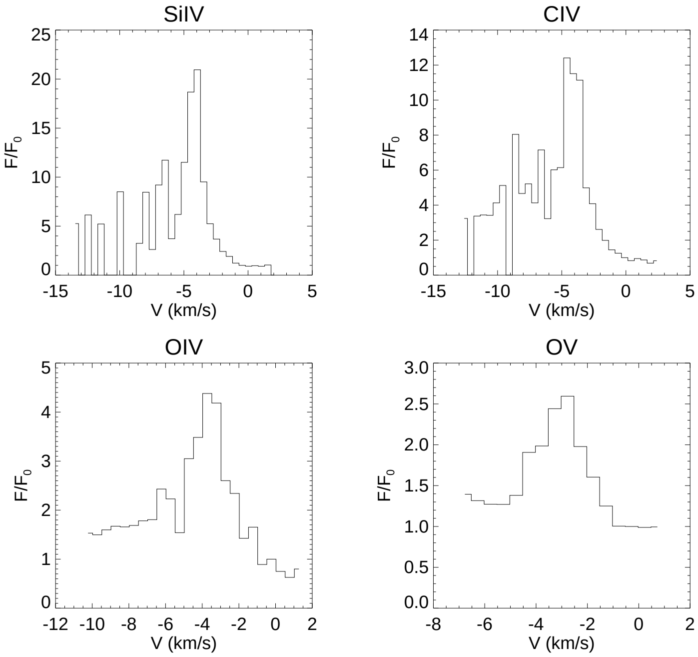
SiIV
CIV
OIV
OV
F/F0
V (km/s)

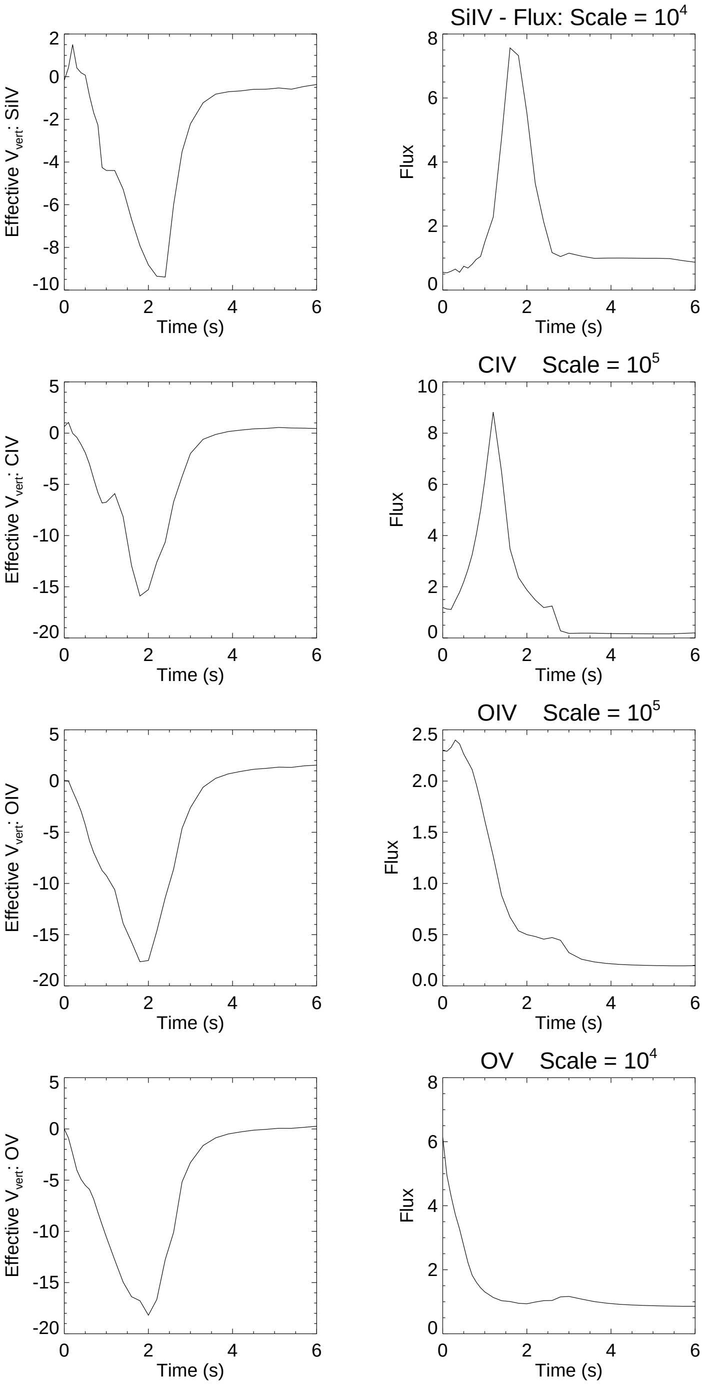
SiIV - Flux: Scale = 10^4
CIV Scale = 10^5
OIV Scale = 10^5
OV Scale = 10^4
Effective V_{vert}: SiIV
Effective V_{vert}: CIV
Effective V_{vert}: OIV
Effective V_{vert}: OV
Flux
Time (s)

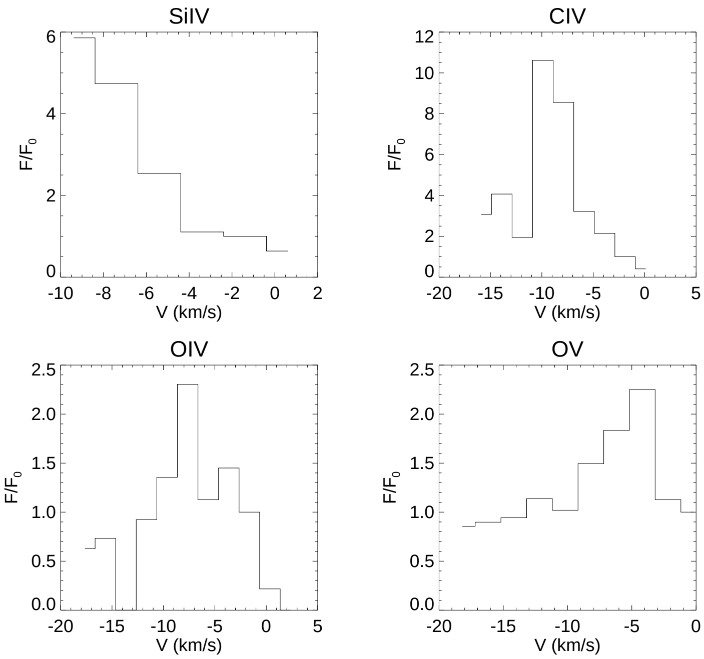
SiIV
CIV
OIV
OV
F/F0
V (km/s)